

kNN-Res: Residual Neural Network with kNN-Graph coherence for point cloud registration

Muhammad S. Battikh^{*1}, Dillon Hammill^{†2}, Matthew Cook^{‡2,3} and
Artem Lensky^{§4}

¹Systems and Computer Engineering Department,
Al-Azhar University, Egypt

²John Curtin School of Medical Research,
The Australian National University, Australia

³Department of Medicine, University of Cambridge, UK

⁴Lensky Analytics

April 4, 2023

Abstract

In this paper, we present a residual neural network-based method for point set registration. Given a target and a reference point cloud, the goal is to learn a minimal transformation that aligns the target to the reference under the constraint that the topological structure of the target point cloud is preserved.

Similar to coherent point drift (CPD), the registration (alignment) problem is viewed as the movement of data points sampled from a target distribution along a regularized displacement vector field. While the coherence constraint in CPD is stated in terms of local motion coherence, the proposed regularization term relies on a global smoothness constraint as a proxy for preserving local topology. This makes CPD less flexible when the deformation is locally rigid but globally non-rigid as in the case of multiple objects and articulate pose registration. To mitigate these issues, a Jacobian-based cost function along with geometric-aware statistical distances is proposed. The latter allows for measuring misalignment between the target and the reference. The justification for the kNN graph preservation of target data, when the Jacobian cost is used, is also provided. Further, a stochastic approximation for high-dimensional registration is introduced to make a high-dimensional alignment feasible. The proposed method is tested on high-dimensional Flow

^{*}muhammad.saeed.batikh@azhar.edu.eg

[†]dillon.hammill@anu.edu.au

[‡]mc2386@cam.ac.uk

[§]artem@lensky.com.au

Cytometry to align two data distributions whilst preserving the kNN-graph of the data. The implementation of the proposed approach is available at https://github.com/MuhammadSaeedBatikh/kNN-Res_Demo/ under the MIT license.

1 Introduction

Point set registration is a widely studied problem in the field of computer vision but also arises in other fields e.g. bioinformatics as is discussed below. The problem involves aligning a deformed target set of d -dimensional points to another reference point set by applying a constrained transformation. This alignment allows for improved comparison and analysis of the two sets of points and is used in a variety of fields including object tracking, body shape modeling, human pose estimation, and removal of batch effects in biological data. [1, 2, 3, 4, 5]

Point set registration techniques are typically categorized based on two main properties, first, whether the technique is a correspondence-based or a correspondence-free technique, and second, whether the estimated transformation is rigid or non-rigid. Correspondence-based techniques require the availability of correspondence information (e.g. labels) between the two point sets, while correspondence-free, sometimes called simultaneous pose and correspondence registration, does not require such information and therefore is considered a significantly more difficult problem. Rigid registration techniques are also generally simpler. A rigid transformation is an isometric transformation that preserves the pairwise distance between points and such transformation is typically modeled as a combination of rotation and translation. Several rigid registration techniques have been proposed in [6, 7, 8, 9, 10, 11, 12, 13, 14]. Assuming the transformation is rigid, however, makes the types of deformations that could be handled quite limited. Non-rigid transformations allow for more flexibility; however, this makes the problem ill-posed as there are an infinite number of transformations that could align two point sets, thus, non-rigid registration techniques employ additional constraints.

1.1 Problem Formulation

In this section, we formulate the alignment problem. Inspired by CPD [15], we view an alignment method as finding a map ϕ that transforms data points sampled from an underlying distribution Q to distribution P in such a way that preserves the topological structure of data sampled from Q . This is an ill-posed density estimation problem, therefore, we require an additional desiderium for ϕ to be as simple as possible. In this context, we call a map ϕ simple if it is close to the identity transformation. Importantly, this could be visualized as data points sampled from Q moving along a regularized displacement vector field F .

More formally, denote two sets of d -dimensional vectors (points), a refer-

ence point set $\mathbf{R} = \{\mathbf{x}_1, \mathbf{x}_2, \dots, \mathbf{x}_n\}$, and target point set $\mathbf{T} = \{\mathbf{y}_1, \mathbf{y}_2, \dots, \mathbf{y}_m\}$, generated by a probability distributions P and Q respectively. Additionally, a k -Nearest Neighbour (kNN) graph is associated with (or constructed from) the set \mathbf{T} which must be preserved after transformation. A kNN graph for set \mathbf{T} is a directed graph such that there is an edge from node i to j if and only if \mathbf{y}_j is among \mathbf{y}_i 's k most similar items in \mathbf{T} under some similarity measure ρ .

Thus, the goal of an alignment method, given the sets \mathbf{R} and \mathbf{T} in a matrix form of $X \in \mathbf{R}^{n \times d}$ and $Y \in \mathbf{R}^{m \times d}$ respectively, is finding a transformation ϕ parameterized by θ such that:

$$\hat{\theta} = \arg \max_{\theta} D(\phi(Y; \theta), X) \quad (1)$$

subject to the constraints:

$$\text{kNN}_g(\phi(Y; \theta)) = \text{kNN}_g(y) \quad (2)$$

where D is a statistical distance that measures the difference between two probability distributions.

1.2 Limitations of existing approaches

A classic example of a such constraint is found in CPD [15] and its extensions [16, 17, 18]. CPD uses a Gaussian Mixture Model to induce a displacement field from the target to source points and uses local motion coherence to constrain the field such that nearby target points move together. CPD achieves this however via a global smoothing constraint which makes it locally inflexible, and therefore unsuitable for articulated deformations in 3D human data, scenes with multiple objects, and biological data [19].

In this work, we introduce a Jacobian orthogonality loss and show that it is a sufficient condition for preserving the kNN graph of the data. Jacobian orthogonality introduced as a penalty $|\mathbf{J}_{\mathbf{X}}^{\top} \mathbf{J}_{\mathbf{X}} - \mathbf{I}_d|$ where $\mathbf{J}_{\mathbf{X}}$ is the Jacobian matrix at a point \mathbf{x} and \mathbf{I}_d is the $d \times d$ identity matrix. The penalty has been proposed in other contexts as well, such as unsupervised disentanglement [20] and medical image registration [21, 22].

In [21], the finite difference method is employed to compute the Jacobian penalty for the B-splines warping transformation, and mutual information of corresponding voxel intensities is used as the similarity measure. Instead of using finite difference for the Jacobian penalty, which produces a numerical approximation of first-order derivatives, the authors of [22] derive an analytical derivative specific to the multidimensional B-splines case. Such approaches however are limited to low dimensions by the nature of the transformations used, the way in which the Jacobian penalty is computed, and their proposed similarity measures.

1.3 Contributions

To address these limitations, we use Hutchinson’s estimator [20, 23] for fast computation of the Jacobian loss for high-dimensional point clouds, a scalable residual neural network (ResNet) [24] architecture as our warping transformation, and geometry-aware statistical distances. The choice of ResNet with identity block $\phi(x) = x + \delta(x)$ is natural since we view alignment similar to CPD as a regularized movement of data points along a displacement vector field; which in our case is simply $\phi(x) - x = \delta(x)$. It is also worth mentioning that ResNets can learn identity mapping more easily. Further discussion on this choice is given in section 2.2. Moment-matching ResNet(MM-Res) [5] use a similar ResNet architecture with RBF kernel maximum-mean discrepancy as its similarity measure [25, 26], however, no topological constraints are provided to preserve the topological structure of the transformed data nor to limit the nature of the learned transformation as shown in Figure 1. Additionally, while maximum-mean discrepancy is a geometry-aware distance, we address some limitations by incorporating Sinkhorn divergence into our framework [27].

To elaborate further, we first start by defining Maximum Mean Discrepancy (MMD):

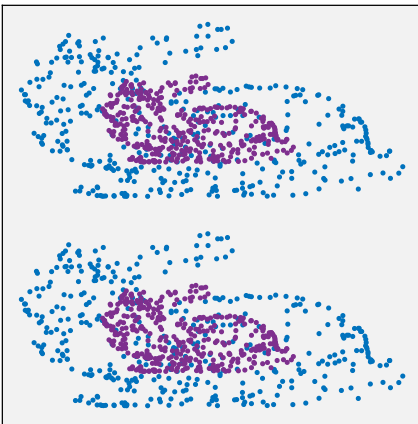
$$\text{MMD}(\alpha, \beta) := \frac{1}{2} \int_{X^2} k(\mathbf{x}, \mathbf{y}) d\zeta(\mathbf{x}) d\zeta(\mathbf{y}) \quad (3)$$

where $\alpha, \beta \in M_1^+(X)$ are unit-mass positive empirical distributions on a feature space X , $\zeta = \alpha - \beta$, and $k(\mathbf{x}, \mathbf{y})$ is a kernel function. **MM-Res** uses an RBF kernel which is suitable for high-dimensional Euclidean feature spaces (e.g. to represent $X \subset \mathbb{R}^n$) and makes training complexity low as it scales up to large batches, nonetheless, such kernel blinds the model to details smaller than its standard deviation, and the networks’ gradient suffers from the well-known vanishing gradient problem. One simple solution is to decrease the standard deviation of the kernel; however, this introduces another issue, namely, the target points will not be properly attracted to source points [28]. In practice, this makes such a framework incapable of learning simple deformations with sizable translations as we show in section 4. Optimal transport (OT) losses do not typically suffer from this issue and produce more stable gradients; however, such losses require solving computationally costly linear programs. A well-known efficient approximation of the OT problem is entropic regularized OT_ϵ [29], for $\epsilon > 0$, it is defined as:

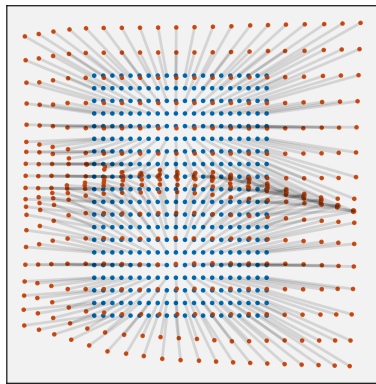
$$\text{OT}_\epsilon(\alpha, \beta) := \min_{\pi_1=\alpha, \pi_2=\beta} \int_{X^2} C(\mathbf{x}, \mathbf{y}) d\pi + \epsilon \text{KL}(\pi | \alpha \times \beta) \quad (4)$$

where C is a cost function (typically the Euclidean distance), (π_1, π_2) denotes the two marginals of the coupling measure $\pi \in M_1^+$ and KL is the KL-divergence. The solution for this formulation could be efficiently computed using the Sinkhorn algorithm as long as $\epsilon > 0$. It is clear that by setting ϵ to 0, this minimization problem reduces back to standard OT. Sinkhorn divergence combines the advantages of MMD and OT and is defined as:

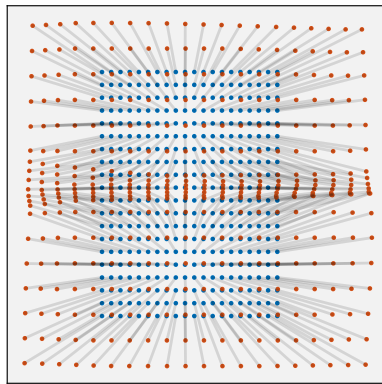
$$S_\epsilon(\alpha, \beta) = \text{OT}_\epsilon(\alpha, \beta) - \frac{1}{2}(\text{OT}_\epsilon(\alpha, \alpha) + \text{OT}_\epsilon(\beta, \beta)) \quad (5)$$



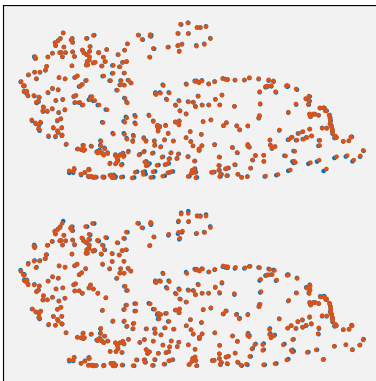
(a) Two bunnies (blue) that have been scaled down from their center by .5 (magenta)



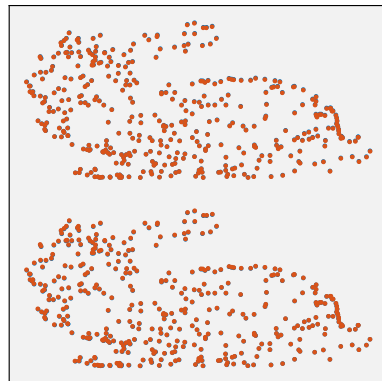
(b) The transformation (grid warping) learned without regularization.



(c) The transformation learned (grid warping) with the Jacobian penalty.



(d) The bunny after transformation (green) without regularization.



(e) The bunny after transformation (green) with regularization.

Figure 1: Stanford Bunny example showing the effect of the Jacobian penalty on the learned transformation.

the authors of [29] show that:

$$\lim_{\epsilon \rightarrow 0} S_{\epsilon}(\alpha, \beta) = \text{OT}(\alpha, \beta) \quad (6)$$

and

$$\lim_{\epsilon \rightarrow \infty} S_{\epsilon}(\alpha, \beta) = \frac{1}{2} \text{MDD}_{-C}^2(\alpha, \beta) \quad (7)$$

where C is the kernel used by MMD.

In the following section, we review other related methods.

1.4 Other related work

Several point cloud registration approaches have been proposed. Thin plate spline functions-based techniques preserve the local topology via local rigidity on the surface of a deformed shape; however, these approaches are not scalable to large datasets and are typically limited to 3-dimensional point clouds [30, 31, 32, 33, 34, 35]. To address these limitations, a deep learning paradigm for point cloud registration has been adopted. Deep learning-based approaches can be divided into two categories, namely, features-based, and end-to-end learning. In features-based methods, a neural network is used as a feature extraction. By developing sophisticated network architectures or loss functions, they aim to estimate robust correspondences by the learned distinctive feature [30, 36, 37, 38]. While feature-based learning typically involves elaborate pipelines with various steps such as feature extraction, correspondence estimation, and registration, end-to-end learning methods combine various steps in one objective and try to solve the registration problem directly by converting it to a regression problem [39, 40]. For example, [39] employs a key point detection method while simultaneously estimating relative pose.

Another class of methods is Graph Matching techniques, which are quadratic assignment problems (QAP) [40]. The main challenge for such methods is finding efficient approximate methods to the otherwise NP-hard QAP. Congruent Sets Gaussian Mixture (CSGM) [41] uses a linear program to solve the graph-matching problem and apply it to solve the cross-source point cloud registration task. Another approach is a high-order graph [42] that uses an integer projection algorithm to optimize the objective function in the integer domain. Finally, Factorized Graph Matching (FGM) method [43] factorizes the large pairwise affinity matrix into some smaller matrices. Then, the graph-matching problem is solved with a simple path following optimization algorithm.

2 Proposed model

2.1 Methodology

In our case, we parametrize the transformation ϕ as a residual neural network and formulate the optimization problem as:

$$\mathcal{L}(\theta) = \mathcal{L}_1 + \lambda \mathcal{L}_2 \quad (8)$$

where \mathcal{L}_1 is the alignmnet loss $D(\theta(Y; \theta), X)$ and λ is a hyperparamater, and \mathcal{L}_2 is the topology preserving loss:

$$\mathcal{L}_2 = \frac{1}{m} \sum_{\mathbf{y} \in T} |\mathbf{J}_X^\top \mathbf{J}_X - \mathbf{I}_d| \quad (9)$$

where \mathbf{J}_y is the Jacobian matrix at points y and \mathbf{I}_d is the $d \times d$ identity matrix. In section 2.4 we prove that the orthogonality of the Jacobian matrix is indeed a sufficient condition for preserving the kNN graph of the data. We use two statistical distances, namely, Sinkhorn divergences, and maximum mean discrepancy. Sinkhorn divergences is a computationally efficient approximation for the Wasserstein distance in high dimensions and converge to the maximum mean discrepancy.

$$\mathcal{L}_1(\theta) = S(\alpha, \beta) = \text{OT}_2(\alpha, \beta) - \frac{1}{2}(\text{OT}_2(\alpha, \alpha) + \text{OT}_2(\beta, \beta)) \quad (10)$$

where OT_ϵ is the optimal transport with \mathcal{L}_2 -norm cost, and α and β are measures over reference and target distributions respectively. The measures α and β are unknown and are only known via samples from \mathbf{R} and \mathbf{T} respectively. Although $S_\epsilon(\alpha, \beta)$ interpolates to MMD as ϵ goes to infinity, we still maintain an efficient standalone MMD distance for data where MMD performs better than the Wasserstein distance and therefore no need for the interpolation overhead. Specifically, we use Gaussian-based MMD:

$$\text{MMD}(\alpha, \beta) := \frac{1}{2} \int_{X^2} k(\mathbf{x}, \mathbf{y}) d\zeta(\mathbf{x}) d\zeta(\mathbf{y}) \quad (11)$$

2.2 Architecture

We use a simple ResNet identity block with a skip connection as our transformation where the output dimension is equal to the input dimension, and the output is calculated as such: $\phi(\mathbf{y}; \theta) = \mathbf{y} + \delta(\mathbf{y}; \theta)$, where δ is a standard multi-layer perceptron (MLP) with **LeakyRelu** activation functions and θ represents the trainable weights of the network. The ResNet identity block has been chosen for two reasons: biasing θ to have small values via weight decay or initializing the output layer using a distribution with mean zero and a small standard deviation minimizes the contribution of $\delta(\mathbf{y}; \theta)$ to the final transformation which makes $\phi(\mathbf{y}; \theta)$ close to the identity. Additionally, this follows the same recipe from CPD of viewing the alignment function as a smooth displacement field.

The ResNet identity block is chosen for the following two reasons. Biasing θ to have small values via weight decay or initialization using a distribution with close to zero values minimizes the contribution of $\delta(\mathbf{x} : \theta)$ to the final transformation which in turn makes $\phi(\mathbf{x} : \theta)$ close to the identity by design. Additionally, since we take a similar approach to CPD by viewing the alignment transformation as a regularized movement of data point along displacement vector field F ; having a ResNet identity block is mathematically convenient since a displacement vector is a difference between the final position $\phi(\mathbf{x} : \theta)$

(transformed point) and the initial position (data point) \mathbf{x} such that $F(\mathbf{x}) = \phi(\mathbf{x} : \theta) - \mathbf{x} = \delta(\mathbf{x} : \theta)$, therefore, we only need to worry about $\delta(\mathbf{x} : \theta)$ instead of $(\phi(\mathbf{x} : \theta) - \mathbf{x})$ absent skip connection.

2.3 Orthogonal Jacobian preserves kNN graph

In this section, we show that the orthogonality of the Jacobian matrix evaluated at data points is a sufficient condition for preserving the kNN graph of the data. A vector-valued function $\mathcal{F} : \mathbb{R}_n \rightarrow \mathbb{R}_n$ preserves the kNN graph of data points $X \in \mathbb{R}_n$ if, for every two points \mathbf{v} and \mathbf{w} that are in some small ϵ -neighborhood of \mathbf{u} , the following holds:

$$\|\mathbf{u} - \mathbf{v}\|_2^2 < \|\mathbf{u} - \mathbf{w}\|_2^2 \rightarrow \|F(\mathbf{u}), F(\mathbf{v})\|_2^2 < \|F(\mathbf{u}), F(\mathbf{w})\|_2^2, \quad (12)$$

where $\|\cdot\|_2^2$ is the squared Euclidian distance. Without loss of generality, we choose two points \mathbf{w}, \mathbf{v} that lie in ϵ neighborhood of point \mathbf{u} and linearize the vector field F around point \mathbf{u} such that:

$$F(\mathbf{x}; \mathbf{u}) \approx F(\mathbf{u}) + \mathbf{J}_{\mathbf{u}}(\mathbf{x} - \mathbf{u}), \quad (13)$$

where $\mathbf{J}_{\mathbf{u}}$ is the Jacobian matrix evaluated at point \mathbf{u} .

The squared distance of \mathbf{u} and \mathbf{v} is:

$$\|\mathbf{u} - \mathbf{v}\|_2^2 = (\mathbf{u} - \mathbf{v})^\top (\mathbf{u} - \mathbf{v}) = \sum_i^n (\mathbf{u}_i - \mathbf{v}_i)^2 \quad (14)$$

Similarly, the squared distance between $F(\mathbf{u}; \mathbf{u})$ and $F(\mathbf{v}; \mathbf{u})$ computes as follows

$$\begin{aligned} \|F(\mathbf{u}; \mathbf{u}) - F(\mathbf{v}; \mathbf{u})\|_2^2 &= (F(\mathbf{u}; \mathbf{u}) - F(\mathbf{v}; \mathbf{u}))^\top (F(\mathbf{u}; \mathbf{u}) - F(\mathbf{v}; \mathbf{u})) \\ &= F(\mathbf{u}) - F(\mathbf{u}) - \mathbf{J}_{\mathbf{u}}(\mathbf{v} - \mathbf{u})^\top (F(\mathbf{u}) - F(\mathbf{u}) - \mathbf{J}_{\mathbf{u}}(\mathbf{v} - \mathbf{u})) \\ &= (\mathbf{J}_{\mathbf{u}}(\mathbf{v} - \mathbf{u}))^\top (\mathbf{J}_{\mathbf{u}}(\mathbf{v} - \mathbf{u})) \\ &= (\mathbf{v} - \mathbf{u})^\top \mathbf{J}_{\mathbf{u}}^\top \mathbf{J}_{\mathbf{u}} (\mathbf{v} - \mathbf{u}) \\ &= (\mathbf{v} - \mathbf{u})^\top (\mathbf{v} - \mathbf{u}) \end{aligned}$$

The last step follows from the orthogonality of $\mathbf{J}_{\mathbf{u}}$ i.e. $(\mathbf{J}_{\mathbf{u}}^\top \mathbf{J}_{\mathbf{u}} = \mathbf{I})$

2.4 Jacobian Loss Via Finite Difference

Given a vector-valued function $F : \mathbb{R}^d \rightarrow \mathbb{R}^d$, a data batch $X \in \mathbb{R}^{m \times d}$, and the Jacobian \mathbf{J}_X of F at points \mathbf{X} is an $\mathbb{R}^{m \times d \times d}$ tensor, it is possible to compute $\mathbf{J}_{\mathbf{X}}$ analytically using autodifferentiation modules, however, such computation is highly inefficient, thus, we use numerical approximation.

Given a d -dimensional vector $\mathbf{x} = [x_1, \dots, x_d]$, the partial first derivative of F with respect to x_i is:

$$\frac{\partial F}{\partial x_i} = \lim_{\epsilon \rightarrow 0} \frac{F(\mathbf{x} + \epsilon e_i) - F(\mathbf{x})}{\epsilon}, \quad (15)$$

where e_i is a standard basis vector (i.e. only the i th component equals 1 and the rest are zero). This could be approximated numerically using a small

Algorithm 1: PyTorch code for Jacobian deviation from Orthogonality at data points z using finite difference method.

```

1  def orth_jacobian_fin_diff(G, z, epsilon = 0.01):
2      '''
3      Input G: Function to compute the Jacobian Penalty for.
4      Input z: (batchsize, d) Input to G that the Jacobian is
5      computed w.r.t.
6      Input epsilon: (default 0.01)
7      Output: mean(|JX⊤JX - Id|)
8      '''
9      batchsize, d = z.shape
10     Gz = G(z).view(-1,1, d).repeat(1,d,1).view(-1,d)
11     I = torch.eye(d).repeat(batchsize, 1, 1)
12     zdz = (z.unsqueeze(-1)+eps*I).transpose(2,1).reshape(-1, d)
13     jac = ((G(zdz)- Gz) / eps).reshape(-1, d, d)
14     blossom = torch.bmm(jac, jac)-I
15     return torch.abs(bloss).mean()

```

ϵ . The Jacobian matrix $\mathbf{J}_{\mathbf{x}}$ is simply $[\frac{\partial F}{\partial x_1}, \dots, \frac{\partial F}{\partial x_d}]$. To ensure the orthogonality of the Jacobian at \mathbf{X} , we minimize the following loss:

$$\mathcal{L}_2 = \frac{1}{m} \sum_{\mathbf{x} \in \mathbf{X}} |\mathbf{J}_{\mathbf{x}}^{\top} \mathbf{J}_{\mathbf{x}} - \mathbf{I}_d| \quad (16)$$

This process could be computed efficiently in a few lines of code as indicated in algorithm 1.

2.5 Training

The training process (algorithm 2) takes advantage of two sets of d -dimensional vectors (points), a reference point set $\mathbf{R} = \{\mathbf{x}_1, \mathbf{x}_2, \dots, \mathbf{x}_n\}$, and target point set $\mathbf{T} = \{\mathbf{y}_1, \mathbf{y}_2, \dots, \mathbf{y}_m\}$. First, we sample points from \mathbf{R} and \mathbf{T} and create two matrices \mathbf{X} and \mathbf{Y} . We feed \mathbf{Y} to the model and obtain $\hat{\mathbf{Y}}$. Under the GMM assumption, we compute the GMM posterior probability as a similarity matrix and estimate \mathcal{L}_1 as the negative log-likelihood. For the Sinkhorn divergence approach, we compute equation (10). We use the `SoftkNN` operator to construct the `kNN` graph for both the input \mathbf{Y} and the output $\hat{\mathbf{Y}}$ and compute \mathcal{L}_2 as the mean squared error between the two. Finally, we use backpropagation by minimizing the loss $\mathcal{L} = \mathcal{L}_1 + \lambda \mathcal{L}_2$ until convergence.

2.6 Stochastic Approximation of Orthogonal Jacobian Loss

Using finite difference to compute the Jacobian for low-dimensional point clouds is efficient, however, the computational cost increases linearly with the dimension of the data. Thus, an approximate estimate with the constant computational cost is introduced.

Algorithm 2: Training kNN-Resnet

Input: \mathbf{R} , and \mathbf{T} pointsets, blurring factor σ , step size ϵ , regularisation λ , and batch size b ;

Output: Trained model

▷ Simple mini-batches of size b from \mathbf{R} and \mathbf{T}

while $(\mathbf{X}, \mathbf{Y}) \in (\mathbf{R}, \mathbf{T})$ *until convergence* **do**

$\phi(\mathbf{Y}) \leftarrow \mathbf{Y} + \delta(\mathbf{Y})$;

if $loss == \text{"sinkhorn"}$ **then**

$\mathcal{L}_1 = S(\mathbf{X}, \phi(\mathbf{Y}); \sigma^2)$;

else

$\mathcal{L}_1 = \text{MMD}(\mathbf{X}, \phi(\mathbf{Y}); \sigma^2)$;

$\mathbf{J}_Y[i, :] = \frac{\delta(\mathbf{Y} + \epsilon e_i) - \delta(\mathbf{Y})}{\epsilon}$;

$\mathcal{L}_2 = \frac{1}{m} \sum_{\mathbf{x} \in \mathbf{X}} |\mathbf{J}_x^\top \mathbf{J}_x - \mathbf{I}_d|$;

$\mathcal{L} = \mathcal{L}_1 + \lambda \mathcal{L}_2$;

▷ backpropagation step

 Minimize(\mathcal{L});

Given a vector-valued function F , and a sample \mathbf{x} , we would like to minimize the following:

$$\mathcal{L}_J(F) = |\mathbf{J}^\top \mathbf{J} \circ (\mathbf{I} - \mathbf{I})|_2 = \sum_{i \neq j} \frac{\partial F_i}{\partial x_j} \frac{\partial F_j}{\partial x_i} \quad (17)$$

Following [20, 23], the Hutchinson’s estimator of $\mathcal{L}_J(F)$ can be approximated as such:

$$\mathcal{L}_J(F) = \text{Var}_r(r_\epsilon^\top (\mathbf{J}^\top \mathbf{J}) r_\epsilon) = \text{Var}_r((\mathbf{J} r_\epsilon)^\top (\mathbf{J} r_\epsilon)) \quad (18)$$

where r_ϵ denotes a scaled Rademacher vector (each entry is either $-\epsilon$ or $+\epsilon$ with equal probability) where $\epsilon > 0$ is a hyperparameter that controls the granularity of the first directional derivative estimate and Var_r is the variance. It is worth noting that this does not guarantee orthonormality, only orthogonality. In practice, however, we find that such an estimator produces comparable results to the standard finite difference method and could be efficiently implemented in Pytorch as shown in algorithm 3.

2.7 Parameters Selection

The proposed model has three main hyperparameters, namely: σ , ϵ , and λ . In the case of Sinkhorn divergence, $\sigma > 0$ is the blur (interpolation) parameter between OT and MMD, with a default value of 0.01 for datasets that lie in the first quadrant of the unit hypercube (minmax normalized data). Decreasing σ has the effect of solving for an exact OT, which typically produces very accurate registration, however, this comes at a slower convergence cost. In the cases where it is more advantageous to use MMD, σ represents the standard deviation of the Gaussian kernel. $\epsilon > 0$ represents the finite difference step size

Algorithm 3: PyTorch code for Hutchinson approximation for Jacobian off-diagonal elements at data points z .

```

1  def stochastic_orth_jacobian(G, z, epsilon = 0.01):
2      '''
3      Input G: Function to compute the Jacobian Penalty for.
4      Input z: (batchsize, d) Input to G that the Jacobian is
5      computed w.r.t.
6      Input k: number of directions to sample (default 5)
7      Input epsilon: (default 0.1)
8      Output: mean(|JXTJX - Id|)
9      '''
10     r = torch.randint(0, 2, size=torch.Size((k, *z.size()))))
11     # r: rademacher random vector
12     r[r == 0] = -1
13     vs = epsilon * r
14     diffs = [G(z + v) - Gz for v in vs]
15     # sfd: stochastic finite diffs
16     sfd = torch.stack(diffs) / epsilon
17     loss = torch.var(sfd, dim=0).max()
18     return loss
19 
```

and controls the radius of topology preservation around each point. It is worth noting that a large epsilon value that covers all data tends to produce globally isomorphic transformations. $\lambda > 0$ is simply a regularization parameter that prioritizes regularization over alignment and is typically less than 0.01. An additional hyperparameter k is introduced when using a stochastic approximation of Jacobian orthogonality for high-dimensional data. This hyperparameter determines the number of Rademacher vectors sampled to estimate the Jacobian orthogonality penalty. Generally, a large k tends to produce a more accurate estimation, however; in practice, $k = 5$ seems to be a sufficient number for the datasets we experimented with.

3 Experiments

In this section, we provide experimental results on several datasets, namely, Chui-Rangarajan synthesized dataset used in [31, 44, 45], and single-cell RNA data used in [5]. The Chui-Rangarajan synthesized dataset is comprised of two shapes; a fish shape, and a Chinese character shape. Each shape is subjected to 5 increasing levels of deformations using an RBF kernel, and each deformation contains 100 different samples. The samples are generated using different RBF coefficients which are sampled from a zero-mean normal distribution with standard deviation σ , whereby increasing σ leads to generally larger deformation.

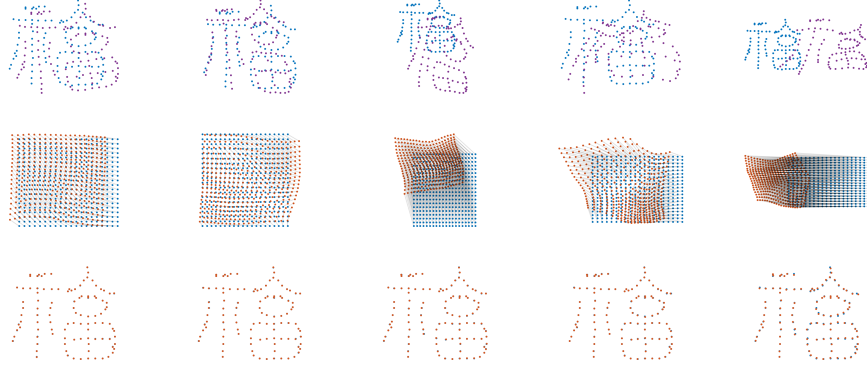


Figure 2: The Chinese character deformation example: Top row represents original and deformed sets, Mid row represents the vector field, and Bottom row is the final alignment.

3.1 Results on 2D Data

We use the root-mean-squared error (RMSE) between the transformed data \hat{y}_i and the ground truth y_i available from the Chui-Rangarajan synthesized dataset:

$$error = \sqrt{\frac{1}{m} \sum_{i=0}^m (\hat{y}_i - y_i)^2}$$

It is important to note that such ground-truth correspondence is absent during training time and is only available during test time. Figures 2 and 3 show the initial point set distributions and their corresponding aligned versions for the Chinese character and the fish examples respectively. We also report results for our kNN-Res, MM-Res[5], CPD [15], TRS-RPM [31], RPM-LNS [45], and GMM-REG [32] over 5 deformation levels and 100 samples per level. Figures 4b and 4b show results for tested models for the Chinese character, and Fish datasets respectively. We notice that after a certain level of non-rigid deformation, MM-Res is unable to converge. For our kNN-Res, we set $\epsilon = .005$, $\lambda = 10^{-5}$, $\sigma = .001$ and number of hidden units = 50. We start with a relatively high learning rate (0.01) for ADAM [46] optimizer and use a reduce-on-plateau scheduler with a reduction factor of 0.7 and minimum learning rate of 5×10^{-5} . Qualitatively, the grid-warp representations from the second column in figures 2 and 3 indicate that our estimated transformations are, at least visually, "simple" and "coherent". Furthermore, to quantitatively assess neighborhood preservation we use the hamming loss \mathcal{L}_H to estimate the difference between the kNN graph before and after transformation:

$$\mathcal{L}_H = \sum_{i=0}^m \sum_{j=0}^m I(\hat{p}_{i,j}^k \neq p_{i,j}^k)$$

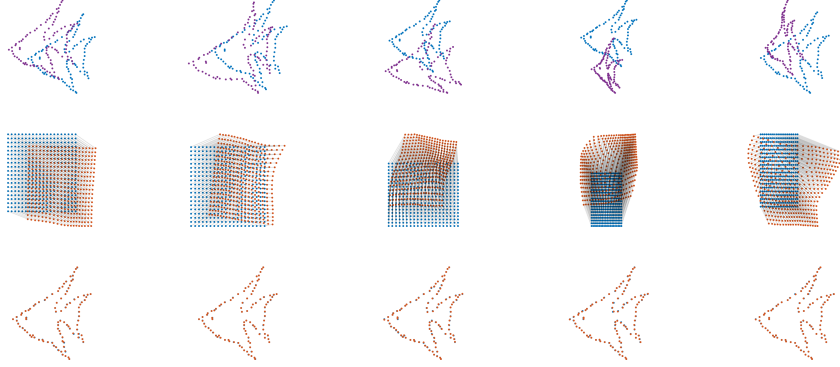


Figure 3: The fish deformation example: Top row represents original and deformed sets, Mid row represents the vector field, and Bottom row is the final alignment.

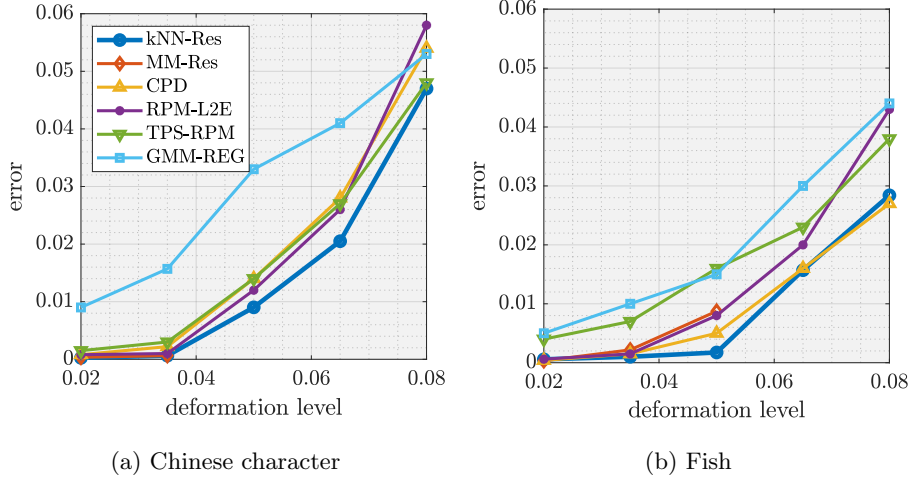


Figure 4: Evaluation metrics

where $p_{i,j}^k$ is the i,j element of the k-NN graph matrix before transformation, $\hat{p}_{i,j}^k$ is the corresponding element after transformation, and I is the indicator function. Figures 5b and 5a show the difference in neighborhood preservation between MM-Res and our kNN-Res for the Chinese character, and Fish datasets respectively for three different levels of deformations.

Moreover, despite the additional topology regularization term, our kNN-Res generally incurred smaller alignment errors and was able to converge under large deformation levels.

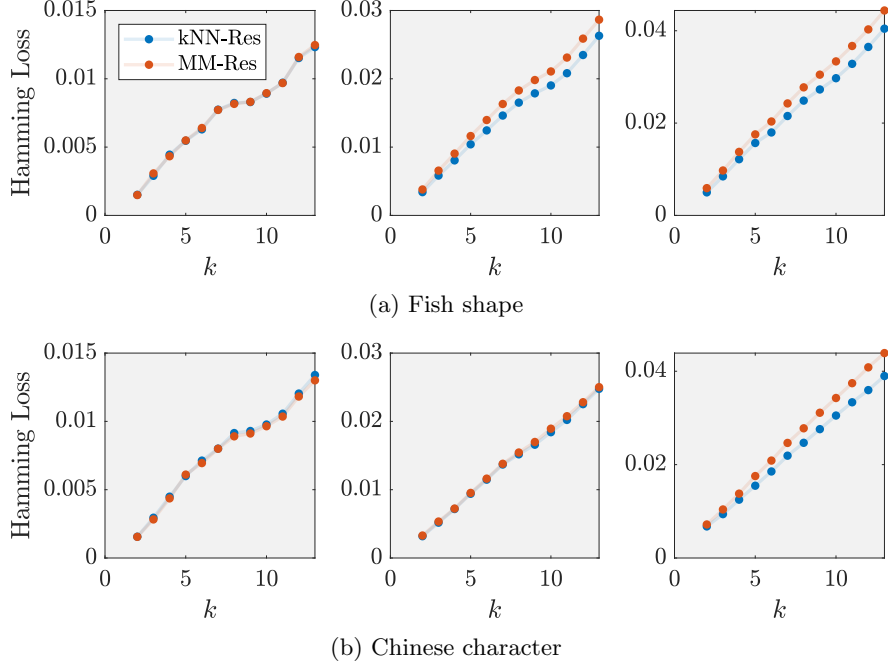


Figure 5: The figures show Hamming loss for the following levels of deformations: (left) level 1, (mid) level 2, (right) level 3.

3.2 Results on High-Dimensional CyTOF Data

Cytometry by time of flight (CyTOF) provides the means for the quantification of multiple cellular components data, however, is susceptible to the so-called batch effect problem, where systematic non-biological variations during the measuring process result in a distributional shift of otherwise similar samples. This effect breaks the intra-comparability of samples which is a crucial component of downstream tasks such as disease diagnosis and typically requires the intervention of human experts to remove these batch effects. The CyTOF dataset used in our experiments was curated by the Yale New Haven Hospital. There are two patients, and two conditions were measured on two different days. All eight samples have 25 markers each representing a separate dimension ('CD45', 'CD19', 'CD127', 'CD4', 'CD8a', 'CD20', 'CD25', 'CD278', 'TNFa', 'Tim3', 'CD27', 'CD14', 'CCR7', 'CD28', 'CD152', 'FOXP3', 'CD45RO', 'INFg', 'CD223', 'GzB', 'CD3', 'CD274', 'HLADR', 'PD1', 'CD11b'), and a range of cells (points) between 1800 to 5000 cells per sample. The split is done such that samples collected on day 1 are the target, and samples collected on day 2 are the reference, resulting in four alignment experiments.

We follow the exact preprocessing steps described in [5]. To adjust the dynamic range of samples, a standard pre-preprocessing step of CyTOF data is

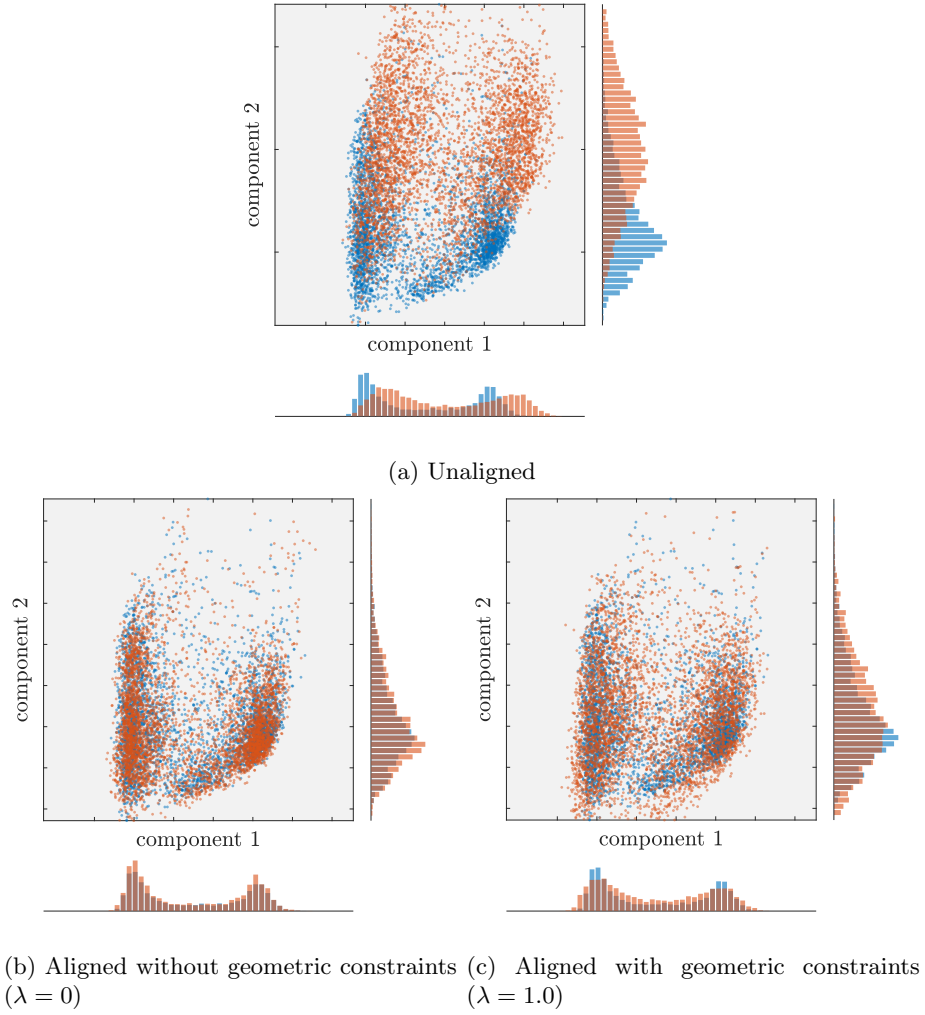


Figure 6: The blue and red dots represent 1st and 2nd principal components of reference (patient #2 on day 2) and the target samples (patient #2 on day 1) correspondingly.

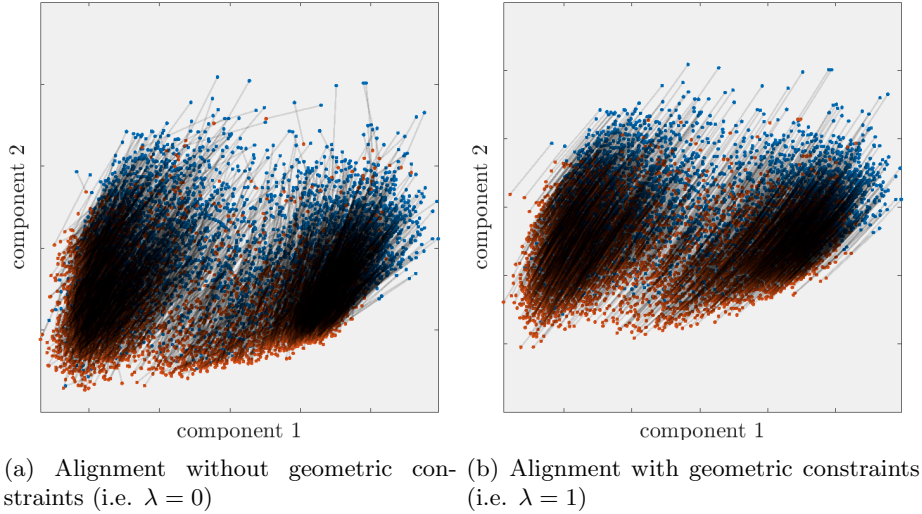


Figure 7: Point set transformation (alignment) of patient #2 sample on day 1 and day 2, shown in space of 1st and 2nd principal components.

applying a log transformation [47]. Additionally, CyTOF data typically contains a large number of zero values (40%) due to instrumental instability which are not considered biological signals. Thus, a denoising autoencoder (DAE) is used to remove these zero-values [48]. The Encoder of the DAE is comprised of two fully-connected layers with ReLU activation functions. The decoder (output) is a single linear layer, with no activation function. All layers of the DAE have the same number of neurons as the dimensionality of the data. Next, each cell is multiplied by an independent Bernoulli random vector with probability = .8, and the DAE is trained to reconstruct the original cell using an MSE loss. Furthermore, the DAE is optimized via RMSprop and weight decay regularization. The zero values in both reference and target are then removed using the trained DAE. Finally, each feature in both target and reference samples is independently standardized to have a zero-mean and unit variance. For our kNN-Res, we set $\epsilon = 0.05$, $\lambda = 0.1$, $\sigma = 0.04$, $k = 5$ for Hutchinson’s estimator, and the number of hidden units to 50. We start with a relatively high learning rate (0.01) for the ADAM optimizer and use a reduce-on-plateau scheduler with a reduction factor of .7, and a minimum learning rate of 5×10^{-5} . Figure 6 shows the first two principal components of data before and after alignment using two kNN-Res models with different lambdas. Although the two samples appear less aligned when using a large λ , this comes with the benefit of preserving the topology of the data as shown by the learned transformation in figure 7 where points (cells) are moved in a coherent way.

This becomes more clearer when looking at the marginals in figure 13 in the appendix. In this experiment, we trained five models with five different

lambdas ranging from 0 to 1. It is clear that having a small λ favors alignment over faithfulness to the original distribution, however, increasing λ preserves the shape of the original data after transformation, which is desirable in biological settings. For results of other experiments see Appendix.

4 Discussion

4.1 Implications

Point-set registration methods are typically used for problems in computer vision to align point clouds produced by either stereo vision or by Light Detection and Ranging devices (e.g. Velodyne scanner) for instance to stitch scenes and align objects. These datasets are usually of 2 or 3 dimensions and hence the methods had limited exposure to high-dimensional datasets. Biological data, on the other hand, is usually of high dimension and hence methods from point-set registration do not directly translate to biological data. The proposed method in this study was tested on a 25-dimensional CyTOF dataset. However, in flow and mass cytometry, data could easily go beyond 50 dimensions (markers). For instance, methods that combine protein marker detection with unbiased transcriptome profiling of single cells provide an even higher number of markers. These methods show that multimodal data analysis can achieve a more detailed characterization of cellular phenotypes than transcriptome measurements alone [49, 50] and hence recently gained significant traction. Unfortunately, these methods require more sophisticated batch normalization algorithms, since manual gating and normalization using marginal distributions become infeasible. It is worth mentioning that even though the experts are making sure that the marginal distributions are aligned, there is still no guarantee that the samples are aligned in the higher dimensional space. Moreover, the alignment might result in such nonlinear and non-smooth transformations that break biological relationships or introduce non-existing biological variabilities. The proposed method mitigates these issues and guarantees smooth transformations.

4.2 Limitations

It is clear from the last step of the proof that the orthogonal Jacobian is too strong a condition for preserving the kNN graph:

$$(\mathbf{v} - \mathbf{u})^\top \mathbf{J}_\mathbf{u}^\top \mathbf{J}_\mathbf{u} (\mathbf{v} - \mathbf{u}) = (\mathbf{v} - \mathbf{u})^\top (\mathbf{v} - \mathbf{u}) \quad (19)$$

The objective is satisfied by preserving inequality and not equality. In other words, it is only necessary and sufficient for \mathbf{J} to preserve the kNN graph if the following holds:

$$\mathbf{u}^\top \mathbf{u} \leq \mathbf{v}^\top \mathbf{v} \rightarrow \mathbf{u}^\top \mathbf{J}^\top \mathbf{J} \mathbf{u} \leq \mathbf{v}^\top \mathbf{J}^\top \mathbf{J} \mathbf{v} \quad (20)$$

or

$$\langle \mathbf{u}, \mathbf{u} \rangle \leq \langle \mathbf{v}, \mathbf{v} \rangle \rightarrow \langle \mathbf{J}\mathbf{u}, \mathbf{J}\mathbf{u} \rangle \leq \langle \mathbf{J}\mathbf{v}, \mathbf{J}\mathbf{v} \rangle \quad (21)$$

Having strict equality puts a limitation on the kind of transformations the model is capable of learning. Furthermore, even if the deformation could theoretically be expressed, such a penalty makes convergence unnecessarily slower. On the empirical side, we only have a limited number of experiments to test the proposed method. More experimentation and ablation are required to better understand the limits of our current approach and to learn how it fairs on a wider selection of real-world data such as RNA-Seq.

4.3 Future Work

An important future direction is incorporating local or partial matching using modified alignment losses such as Gromov-Wasserstein distance. This should lead to a much more robust solution than global matching, especially in the case of outliers and missing objects. We also posit that solving point set registration under topological constraints such as preserving the kNN graph is naturally extendable to dimensionality reduction.

5 Conclusion

This paper presents a simple, scalable framework for point cloud registration. At its core, it consists of three components, namely (a) residual neural network with identity blocks as a parametrized displacement field, (b) Jacobian penalty as a topology-preserving loss, and (c) Sinkhorn Divergence as a sample-based, geometry-aware statistical distance. Additionally, by incorporating Hutchinson’s estimator for the Jacobian loss, we show that our model is easily extensible to high dimensions with constant complexity. Furthermore, we offer both qualitative and quantitative analysis for synthetic and CyTOF datasets showing the flexibility and applicability of our model in multiple domains.

References

- [1] Xiaoshui Huang, Guofeng Mei, Jian Zhang, and Rana Abbas. A comprehensive survey on point cloud registration. *arXiv preprint arXiv:2103.02690*, 2021.
- [2] Alexander Weiss, David Hirshberg, and Michael J Black. Home 3d body scans from noisy image and range data. In *2011 International Conference on Computer Vision*, pages 1951–1958. IEEE, 2011.
- [3] Mao Ye, Xianwang Wang, Ruigang Yang, Liu Ren, and Marc Pollefeys. Accurate 3d pose estimation from a single depth image. In *2011 International Conference on Computer Vision*, pages 731–738. IEEE, 2011.
- [4] Paul Viola and William M Wells. Alignment by maximization of mutual information. In *Proceedings of IEEE International Conference on Computer Vision*, pages 16–23. IEEE, 1995.

- [5] Uri Shaham, Kelly P Stanton, Jun Zhao, Huamin Li, Khadir Raddassi, Ruth Montgomery, and Yuval Kluger. Removal of batch effects using distribution-matching residual networks. *Bioinformatics*, 33(16):2539–2546, 2017.
- [6] Lisa Gottesfeld Brown. A survey of image registration techniques. *ACM computing surveys (CSUR)*, 24(4):325–376, 1992.
- [7] Paul J Besl and Neil D McKay. Method for registration of 3-d shapes. In *Sensor fusion IV: control paradigms and data structures*, volume 1611, pages 586–606. Spie, 1992.
- [8] Szymon Rusinkiewicz and Marc Levoy. Efficient variants of the icp algorithm. In *Proceedings Third International Conference on 3-D Digital Imaging and Modeling*, pages 145–152. IEEE, 2001.
- [9] Sébastien Granger and Xavier Pennec. Multi-scale em-icp: A fast and robust approach for surface registration. In *Computer Vision—ECCV 2002: 7th European Conference on Computer Vision Copenhagen, Denmark, May 28–31, 2002 Proceedings, Part IV* 7, pages 418–432. Springer, 2002.
- [10] Andrew W Fitzgibbon. Robust registration of 2d and 3d point sets. *Image and Vision Computing*, 21(13-14):1145–1153, 2003.
- [11] Niloy J Mitra, Natasha Gelfand, Helmut Pottmann, and Leonidas Guibas. Registration of point cloud data from a geometric optimization perspective. In *Proceedings of the 2004 Eurographics/ACM SIGGRAPH symposium on Geometry processing*, pages 22–31, 2004.
- [12] Ameesh Makadia, Alexander Patterson, and Kostas Daniilidis. Fully automatic registration of 3d point clouds. In *2006 IEEE Computer Society Conference on Computer Vision and Pattern Recognition (CVPR’06)*, volume 1, pages 1297–1304. IEEE, 2006.
- [13] Yuehaw Khoo and Ankur Kapoor. Non-iterative rigid 2d/3d point-set registration using semidefinite programming. *IEEE Transactions on Image Processing*, 25(7):2956–2970, 2016.
- [14] Jiaolong Yang, Hongdong Li, Dylan Campbell, and Yunde Jia. Go-icp: A globally optimal solution to 3d icp point-set registration. *IEEE Transactions on Pattern Analysis and Machine Intelligence*, 38(11):2241–2254, 2015.
- [15] Andriy Myronenko and Xubo Song. Point set registration: Coherent point drift. *IEEE Transactions on Pattern Analysis and Machine Intelligence*, 32(12):2262–2275, 2010.
- [16] Andriy Myronenko, Xubo Song, and Miguel Carreira-Perpinan. Non-rigid point set registration: Coherent point drift. *Advances in Neural Information Processing Systems*, 19, 2006.

- [17] Osamu Hirose. A bayesian formulation of coherent point drift. *IEEE Transactions on Pattern Analysis and Machine Intelligence*, 43(7):2269–2286, 2020.
- [18] Osamu Hirose. Acceleration of non-rigid point set registration with down-sampling and gaussian process regression. *IEEE Transactions on Pattern Analysis and Machine Intelligence*, 43(8):2858–2865, 2020.
- [19] Song Ge, Guoliang Fan, and Meng Ding. Non-rigid point set registration with global-local topology preservation. In *Proceedings of the IEEE Conference on Computer Vision and Pattern Recognition Workshops*, pages 245–251, 2014.
- [20] Yuxiang Wei, Yupeng Shi, Xiao Liu, Zhilong Ji, Yuan Gao, Zhongqin Wu, and Wangmeng Zuo. Orthogonal jacobian regularization for unsupervised disentanglement in image generation. In *Proceedings of the IEEE/CVF International Conference on Computer Vision*, pages 6721–6730, 2021.
- [21] Torsten Rohlfing, Calvin R Maurer, David A Bluemke, and Michael A Jacobs. Volume-preserving nonrigid registration of mr breast images using free-form deformation with an incompressibility constraint. *IEEE Transactions on Medical Imaging*, 22(6):730–741, 2003.
- [22] Dirk Loeckx, Frederik Maes, Dirk Vandermeulen, and Paul Suetens. Non-rigid image registration using free-form deformations with a local rigidity constraint. In *Medical Image Computing and Computer-Assisted Intervention–MICCAI 2004: 7th International Conference, Saint-Malo, France, September 26-29, 2004. Proceedings, Part I 7*, pages 639–646. Springer, 2004.
- [23] Michael F Hutchinson. A stochastic estimator of the trace of the influence matrix for laplacian smoothing splines. *Communications in Statistics-Simulation and Computation*, 18(3):1059–1076, 1989.
- [24] Kaiming He, Xiangyu Zhang, Shaoqing Ren, and Jian Sun. Deep residual learning for image recognition. In *Proceedings of the IEEE Conference on Computer Vision and Pattern Recognition*, pages 770–778, 2016.
- [25] Arthur Gretton, Karsten Borgwardt, Malte Rasch, Bernhard Schölkopf, and Alex Smola. A kernel method for the two-sample-problem. *Advances in Neural Information Processing Systems*, 19, 2006.
- [26] Arthur Gretton, Karsten M Borgwardt, Malte J Rasch, Bernhard Schölkopf, and Alexander Smola. A kernel two-sample test. *The Journal of Machine Learning Research*, 13(1):723–773, 2012.
- [27] Aaditya Ramdas, Nicolás García Trillos, and Marco Cuturi. On wasserstein two-sample testing and related families of nonparametric tests. *Entropy*, 19(2):47, 2017.

- [28] Jean Feydy, Thibault Séjourné, François-Xavier Vialard, Shun-ichi Amari, Alain Trounev, and Gabriel Peyré. Interpolating between optimal transport and mmd using sinkhorn divergences. In *The 22nd International Conference on Artificial Intelligence and Statistics*, pages 2681–2690. PMLR, 2019.
- [29] Christian Léonard. A survey of the schrodinger problem and some of its connections with optimal transport. *arXiv preprint arXiv:1308.0215*, 2013.
- [30] Haili Chui and Anand Rangarajan. A feature registration framework using mixture models. In *Proceedings IEEE Workshop on Mathematical Methods in Biomedical Image Analysis. MMBIA-2000 (Cat. No. PR00737)*, pages 190–197. IEEE, 2000.
- [31] Haili Chui and Anand Rangarajan. A new point matching algorithm for non-rigid registration. *Computer Vision and Image Understanding*, 89(2-3):114–141, 2003.
- [32] Bing Jian and Baba C Vemuri. Robust point set registration using gaussian mixture models. *IEEE Transactions On Pattern Analysis and Machine Intelligence*, 33(8):1633–1645, 2010.
- [33] Jun Chen, Jiayi Ma, Changcai Yang, Li Ma, and Sheng Zheng. Non-rigid point set registration via coherent spatial mapping. *Signal Processing*, 106:62–72, 2015.
- [34] Yang Yang, Sim Heng Ong, and Kelvin Weng Chiong Foong. A robust global and local mixture distance based non-rigid point set registration. *Pattern Recognition*, 48(1):156–173, 2015.
- [35] Xueli Xu, Kang Li, Yifei Ma, Guohua Geng, Jingyu Wang, Mingquan Zhou, and Xin Cao. Feature-preserving simplification framework for 3d point cloud. *Scientific Reports*, 12(1):9450, 2022.
- [36] Andy Zeng, Shuran Song, Matthias Nießner, Matthew Fisher, Jianxiong Xiao, and Thomas Funkhouser. 3dmatch: Learning local geometric descriptors from rgb-d reconstructions. In *Proceedings of the IEEE Conference on Computer Vision and Pattern Recognition*, pages 1802–1811, 2017.
- [37] Haowen Deng, Tolga Birdal, and Slobodan Ilic. Ppfnet: Global context aware local features for robust 3d point matching. In *Proceedings of the IEEE conference on computer vision and pattern recognition*, pages 195–205, 2018.
- [38] Zan Gojcic, Caifa Zhou, Jan D Wegner, and Andreas Wieser. The perfect match: 3d point cloud matching with smoothed densities. In *Proceedings of the IEEE/CVF Conference on Computer Vision and Pattern Recognition*, pages 5545–5554, 2019.

- [39] Riccardo Marin, Simone Melzi, Emanuele Rodola, and Umberto Castellani. High-resolution augmentation for automatic template-based matching of human models. *2019 International Conference on 3D Vision (3DV)*, Oct 2019.
- [40] Eliane Maria Loiola, Nair Maria Maia De Abreu, Paulo Oswaldo Boaventura-Netto, Peter Hahn, and Tania Querido. A survey for the quadratic assignment problem. *European Journal of Operational research*, 176(2):657–690, 2007.
- [41] Xiaoshui Huang, Jian Zhang, Lixin Fan, Qiang Wu, and Chun Yuan. A systematic approach for cross-source point cloud registration by preserving macro and micro structures. *IEEE Transactions on Image Processing*, 26(7):3261–3276, 2017.
- [42] Olivier Duchenne, Francis Bach, In-So Kweon, and Jean Ponce. A tensor-based algorithm for high-order graph matching. *IEEE Transactions On Pattern Analysis and Machine Intelligence*, 33(12):2383–2395, 2011.
- [43] Feng Zhou and Fernando De la Torre. Factorized graph matching. *IEEE Transactions On Pattern Analysis and Machine Intelligence*, 38(9):1774–1789, 2015.
- [44] Yefeng Zheng and David Doermann. Robust point matching for nonrigid shapes by preserving local neighborhood structures. *IEEE Transactions on Pattern Analysis and Machine Intelligence*, 28(4):643–649, 2006.
- [45] Jiayi Ma, Ji Zhao, Jinwen Tian, Zhuowen Tu, and Alan L Yuille. Robust estimation of nonrigid transformation for point set registration. In *Proceedings of the IEEE Conference On Computer Vision and Pattern Recognition*, pages 2147–2154, 2013.
- [46] Diederik P Kingma and Jimmy Ba. Adam: A method for stochastic optimization. *arXiv preprint arXiv:1412.6980*, 2014.
- [47] Rachel Finck, Erin F Simonds, Astraea Jager, Smita Krishnaswamy, Karen Sachs, Wendy Fantl, Dana Pe’er, Garry P Nolan, and Sean C Bendall. Normalization of mass cytometry data with bead standards. *Cytometry Part A*, 83(5):483–494, 2013.
- [48] Pascal Vincent, Hugo Larochelle, Yoshua Bengio, and Pierre-Antoine Manzagol. Extracting and composing robust features with denoising autoencoders. In *Proceedings of the 25th International Conference on Machine Learning*, pages 1096–1103, 2008.
- [49] Marlon Stoeckius, Christoph Hafemeister, William Stephenson, Brian Houck-Loomis, Pratip K Chattopadhyay, Harold Swerdlow, Rahul Satija, and Peter Smibert. Simultaneous epitope and transcriptome measurement in single cells. *Nature Methods*, 14(9):865–868, 2017.

- [50] Vanessa M Peterson, Kelvin Xi Zhang, Namit Kumar, Jerelyn Wong, Lixia Li, Douglas C Wilson, Renee Moore, Terrill K McClanahan, Svetlana Sadekova, and Joel A Klappenbach. Multiplexed quantification of proteins and transcripts in single cells. *Nature Biotechnology*, 35(10):936–939, 2017.

Appendix A CyTOF

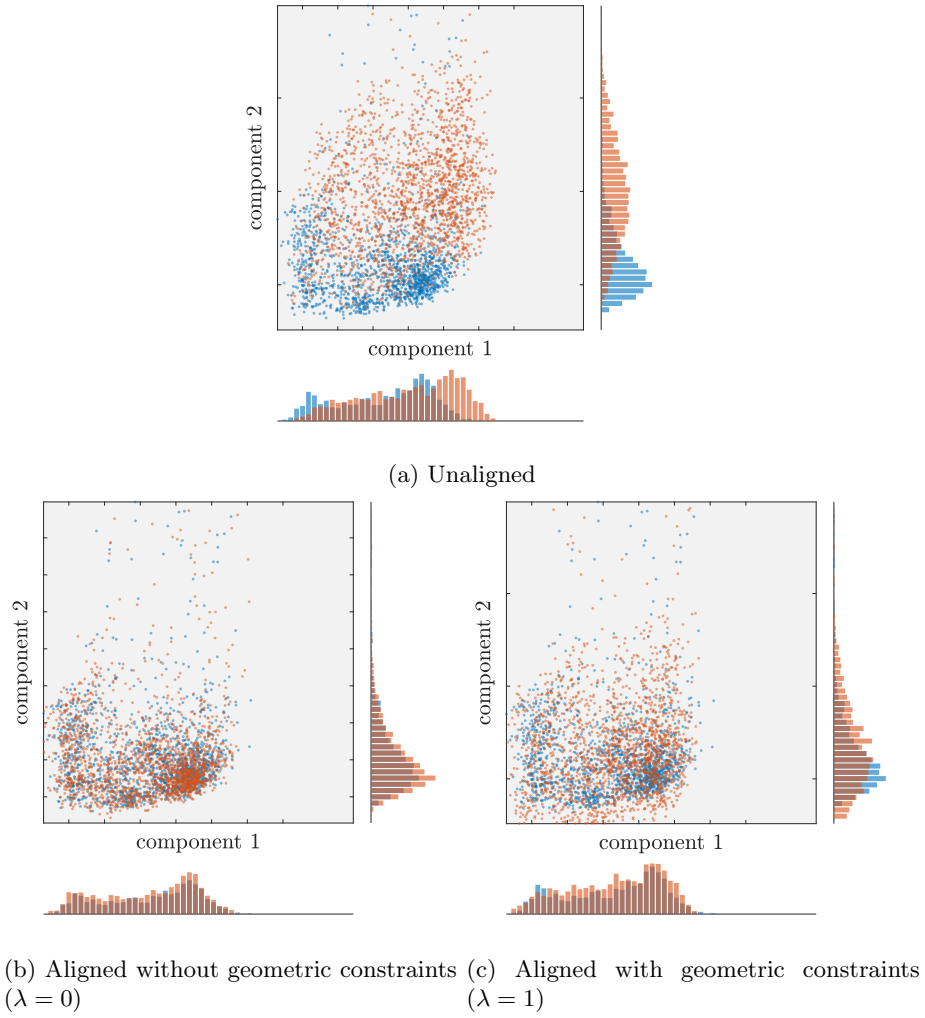


Figure 8: The blue and red dots represent 1st and 2nd principal components of reference (patient #1 on day 2) and the target samples (patient #1 on day 1) correspondingly.

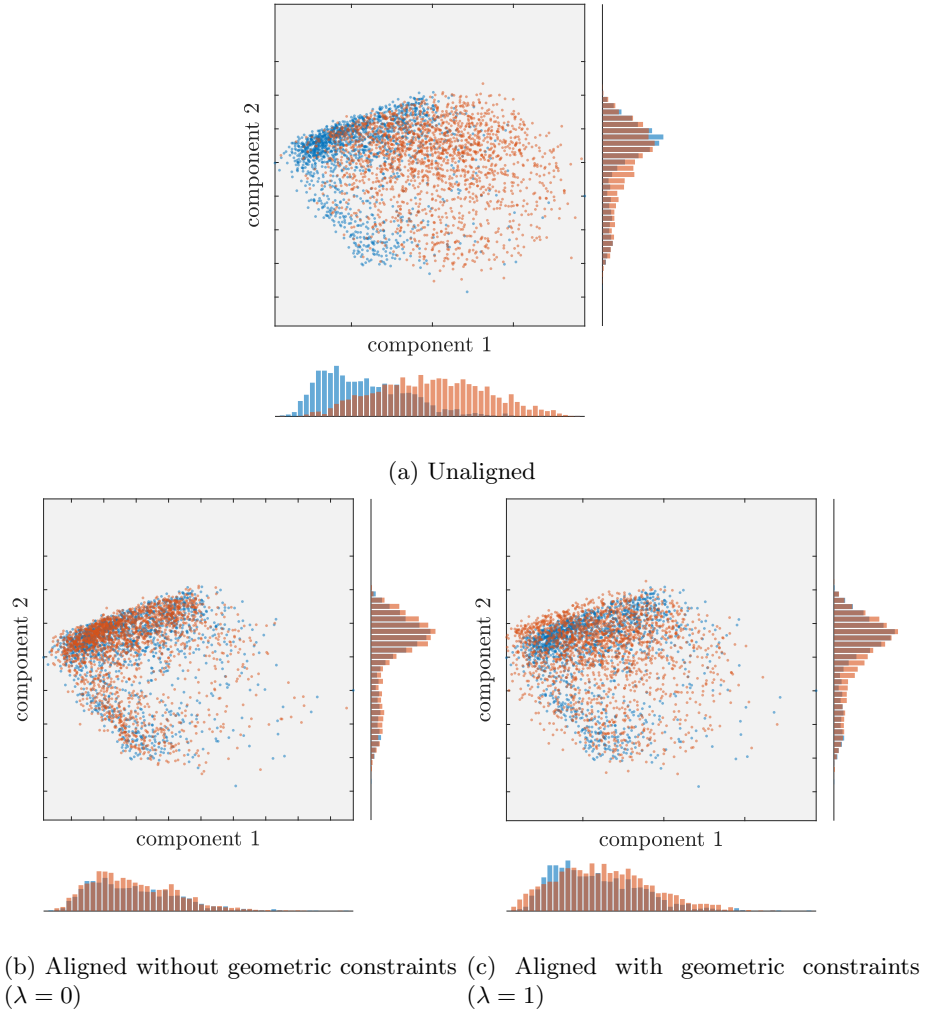


Figure 9: The blue and red dots represent 1st and 2nd principal components of reference (3 months later patient #1 on day 2) and the target samples (3 months later patient #1 on day 1) correspondingly.

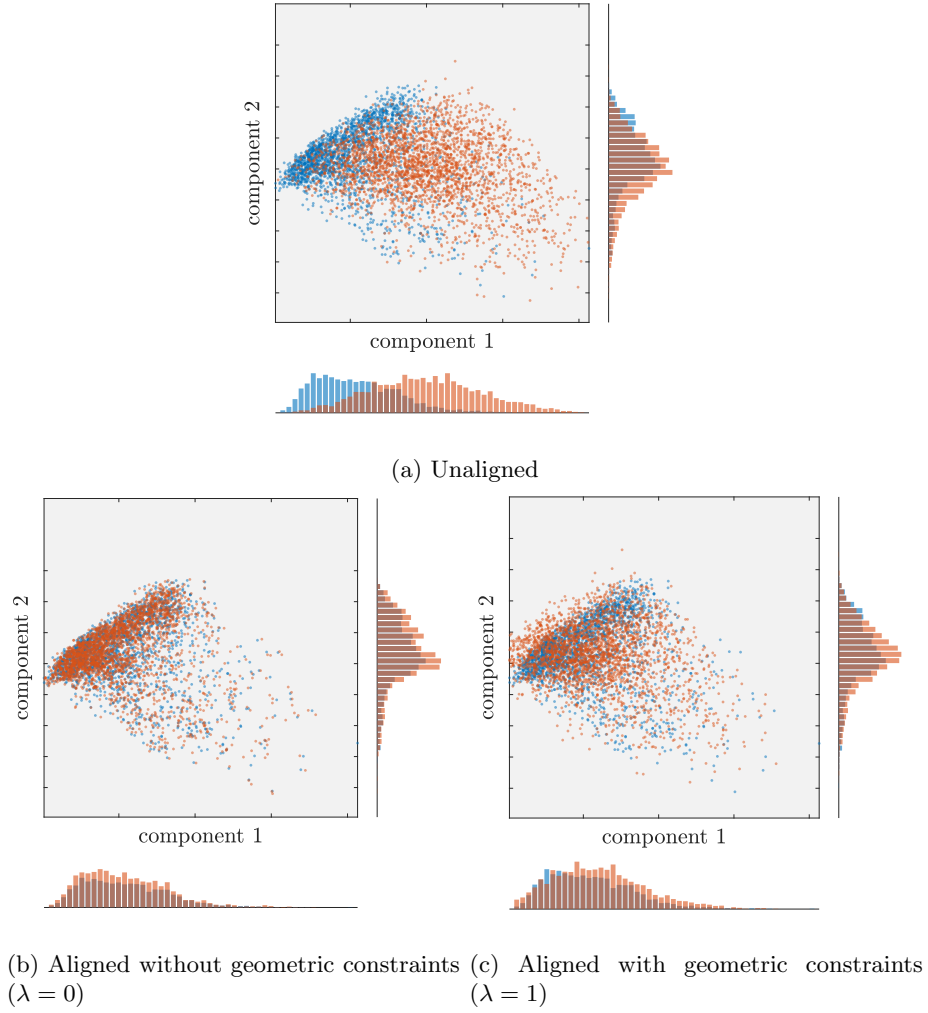


Figure 10: The blue and red dots represent 1st and 2nd principal components of reference (3 months later patient #2 on day 2) and the target samples (3 months later patient #2 on day 1) correspondingly.

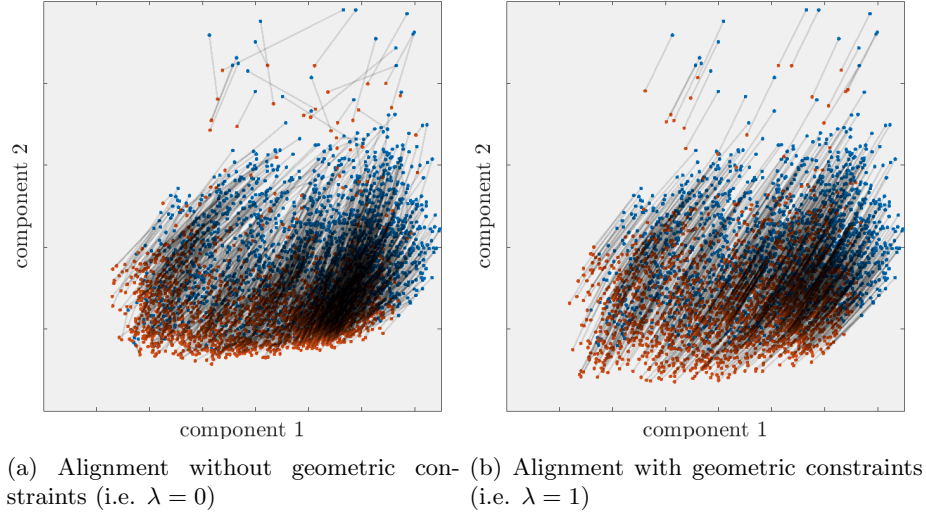


Figure 11: Point set transformation(alignment) of patient #1 sample on day 1 and day 2, shown in space of 1st and 2nd principal components.

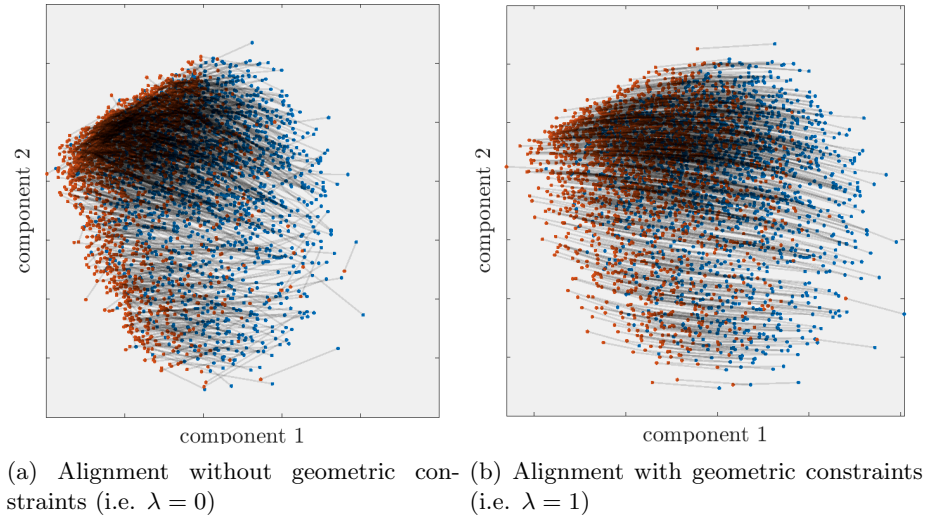


Figure 12: Point set transformation(alignment) of patient #1, 3 months later sample on day 1 and day 2, shown in space of 1st and 2nd principal components.

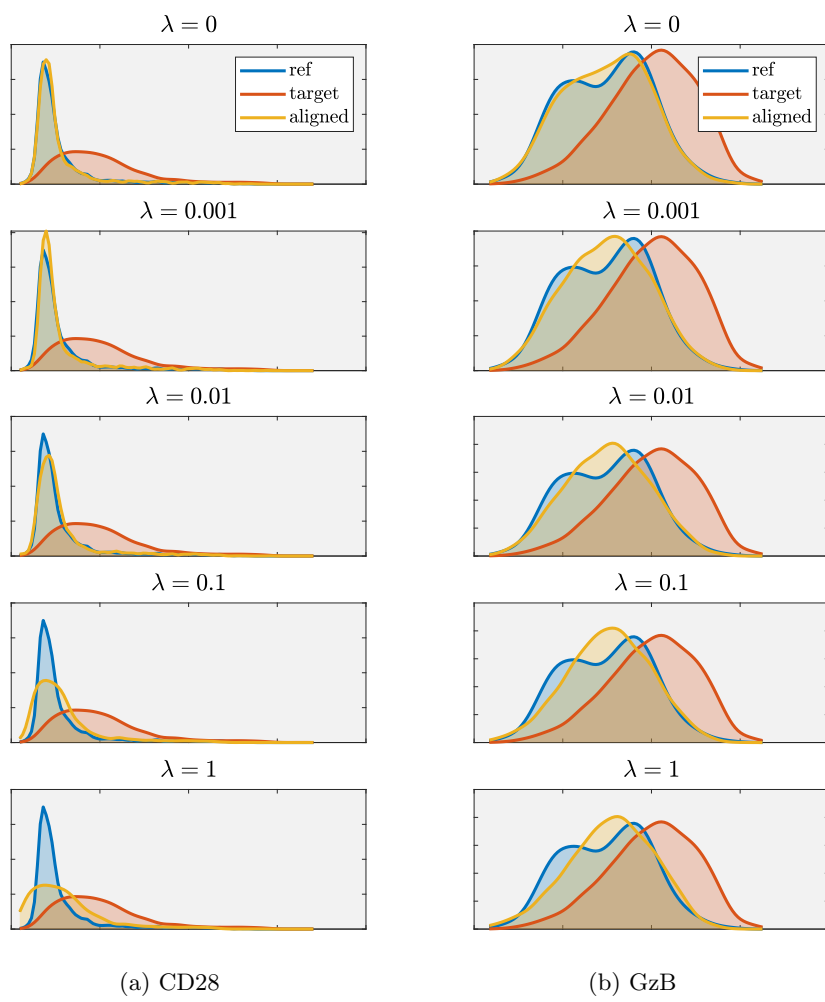


Figure 13: Marginals